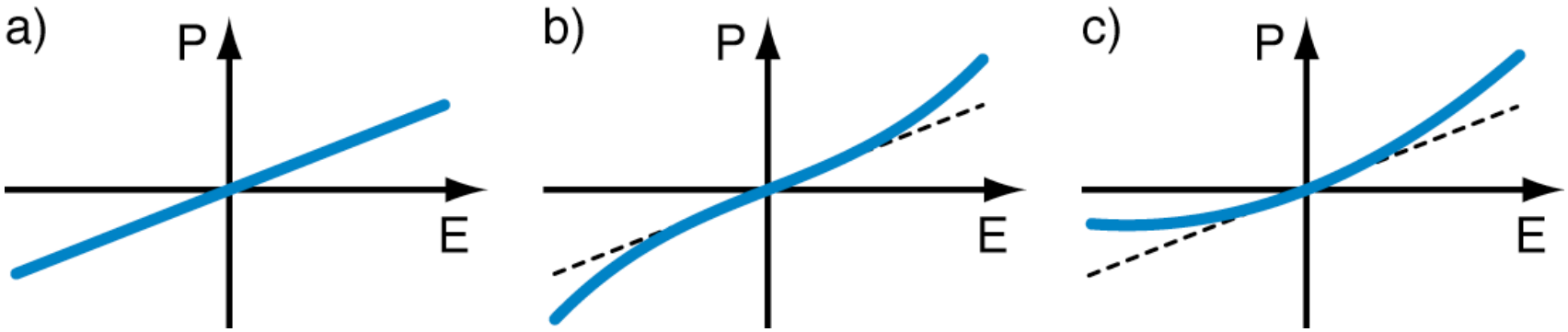

Figure15.1 Induced polarization *P* in dielectrics for a) linear medium, b) nonlinear centrosymmetric medium, and c) nonlinear noncentrosymmetric medium.

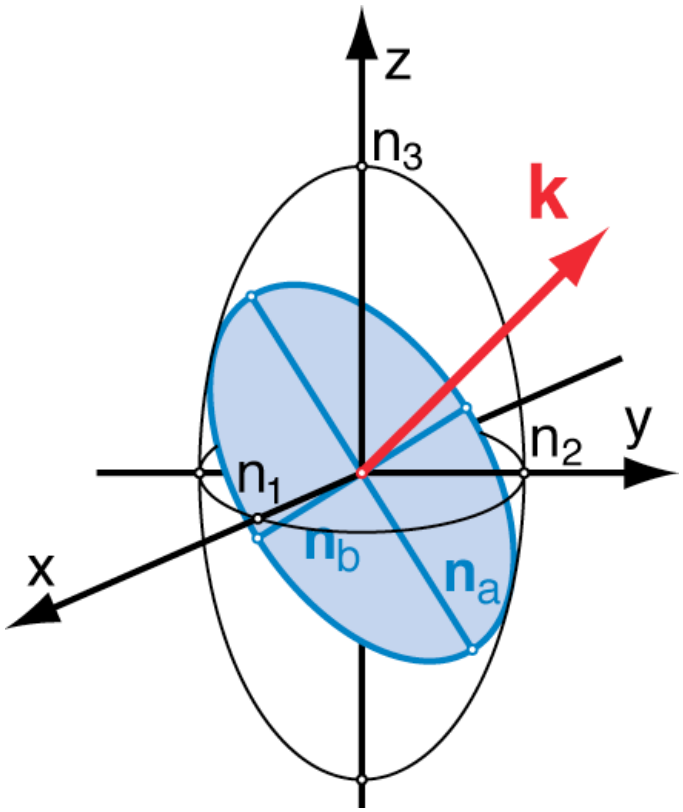

Figure15.2 Optical indicatrix in the principal-axes system $x_1x_2x_3$. The refractive indices of the two normal modes for a wave traveling in the direction **k** are n_a and n_b. The polarizations of these two modes are parallel to the major and the minor axis of the intersection ellipse respectively.

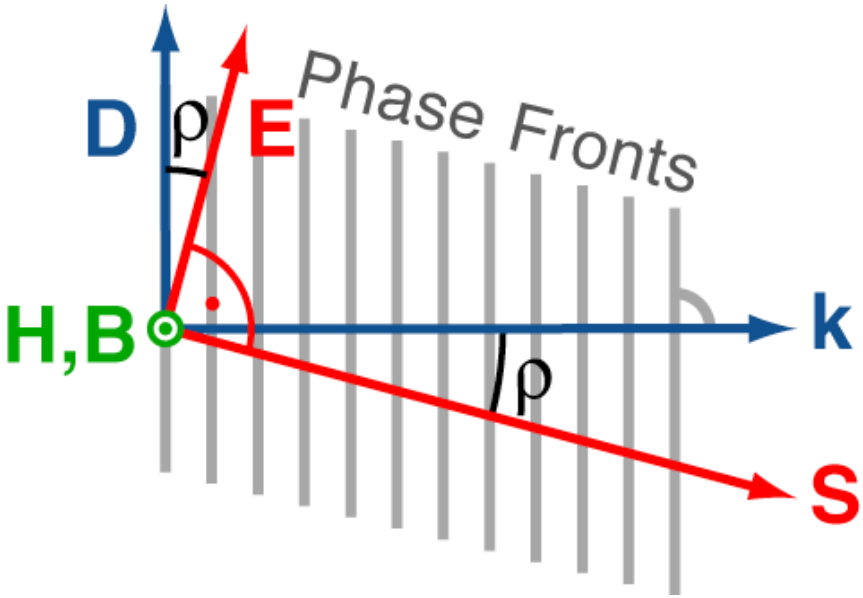

Figure15.3 Directions of electromagnetic fields **D**, **E**, **H**, and **B**, phase propagation direction **k**, and energy propagation direction **S** in an anisotropic medium. The vectors **D**, **E**, **k**, and **S** lie in the plane to which **H** and **B** are normal. The angle between the energy and the phase propagation direction is denoted by ρ and equals to the angle between **E** and **D**.

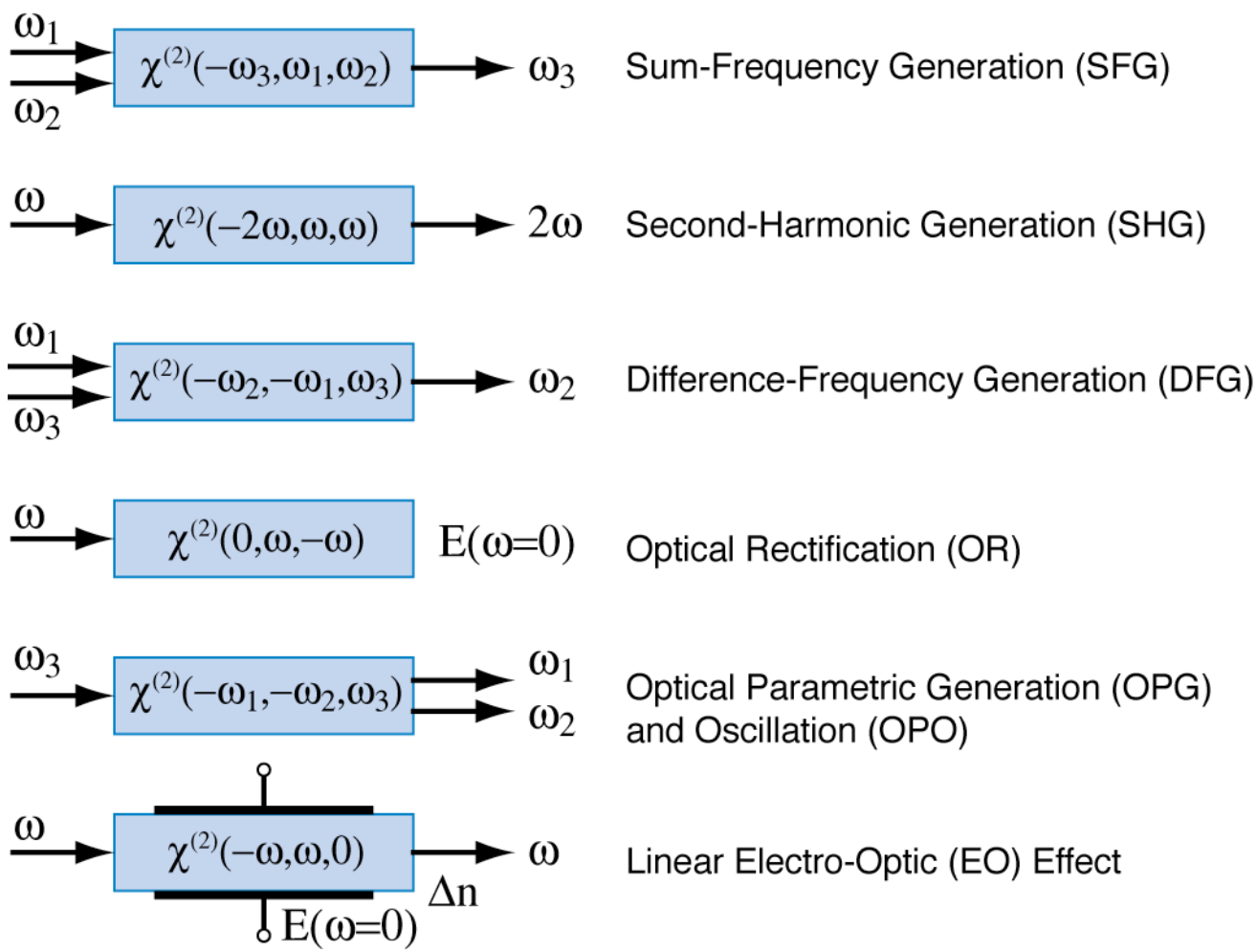

Figure15.4 Schematic representation of important nonlinear optical effects of the second-order, including the linear electro-optic effect.

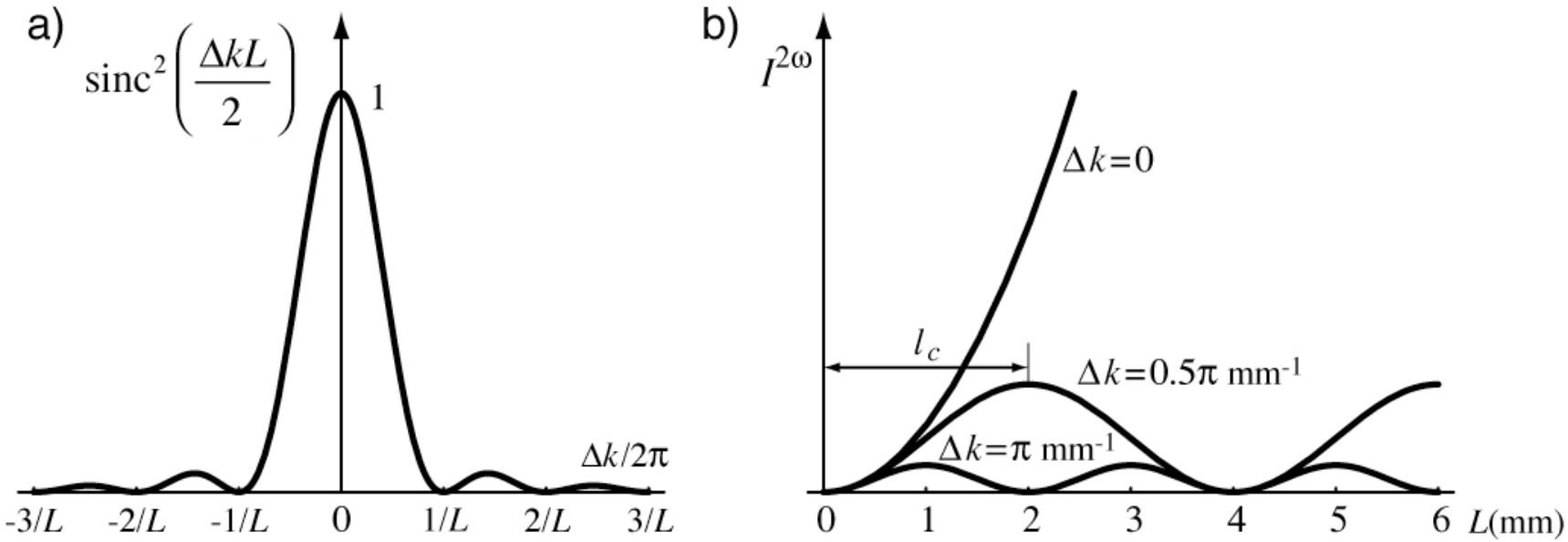

Figure15.5 a) Factor that reduces the efficiency of the second harmonic generation due to the phase mismatch Δk. b) Second-harmonic intensity as a function of the crystal thickness for different values of the phase mismatch Δk.

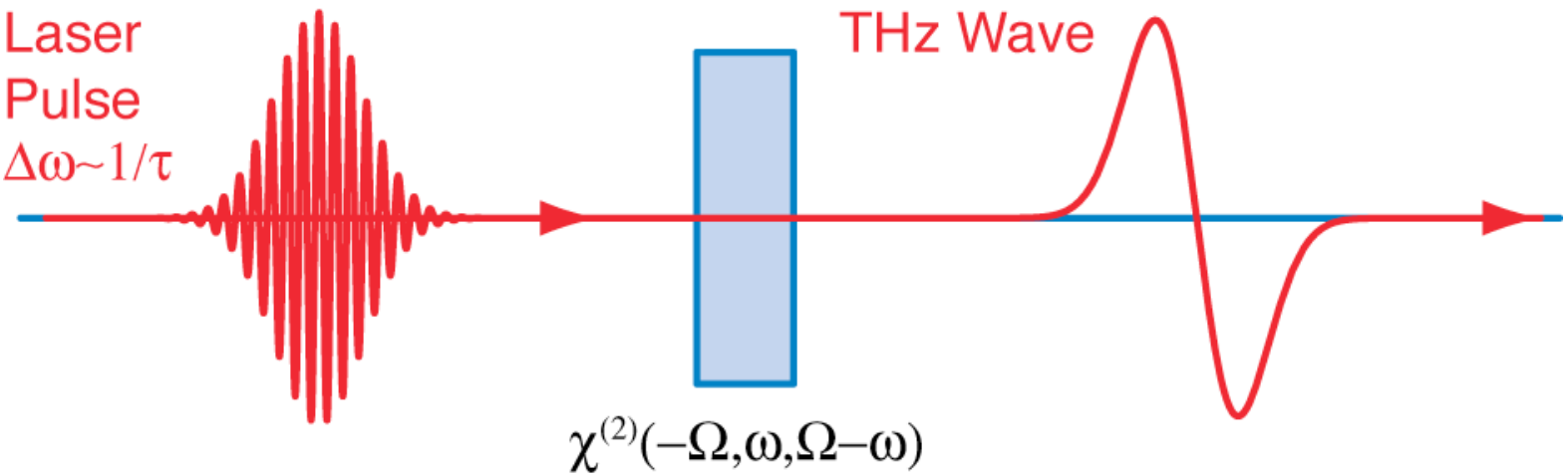

Figure15.6 Schematic illustration of THz wave generation via optical rectification in a second-order nonlinear optical crystal. Initial ultrashort optical pulse (τ ~ 100 fs) contains several frequency components that are mixing with each other in the crystal to generate a nonlinear polarization oscillating in the THz frequency range.

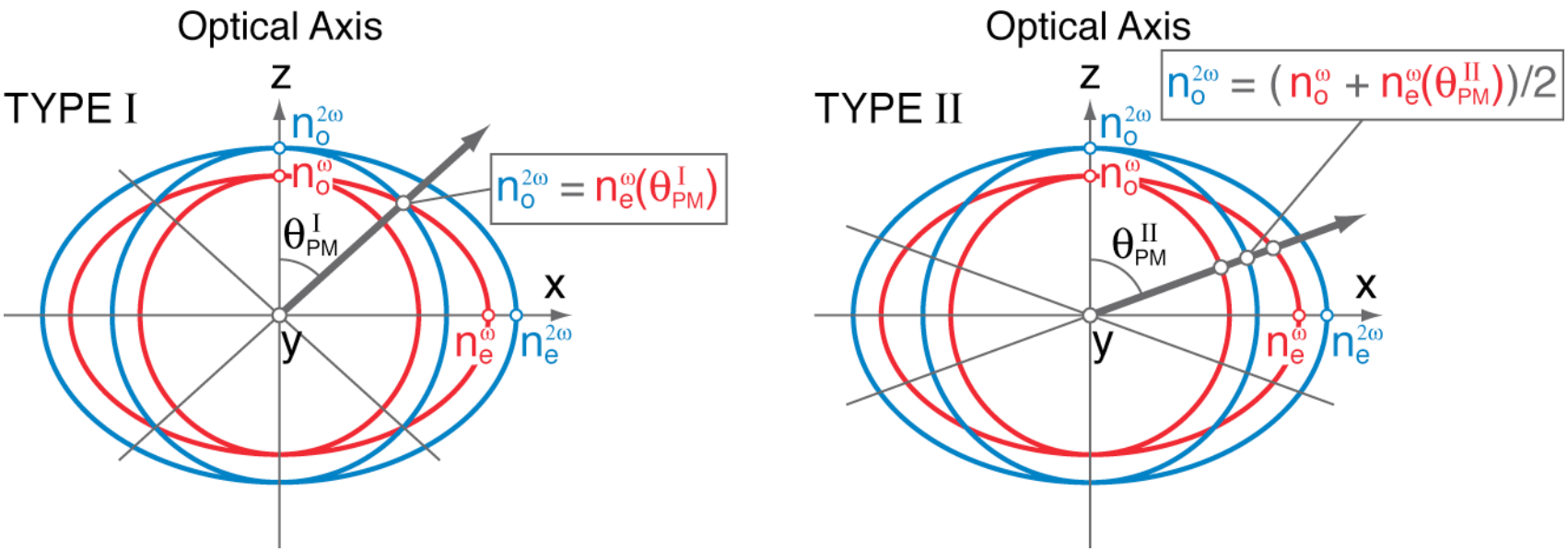

Figure15.7 Type I (left) and Type II (right) phase matching for a uniaxial crystal with $n_e > n_o$. The curves (circles, ellipses) are the so-called normal surfaces of the two orthogonal eigenwaves at ω (solid curves) and at 2ω (dotted curves), which give the refractive index as a function of the propagation direction (the direction of the wavevector **k**). The normal surfaces can be constructed from the optical indicatrix according to Figure15.2.

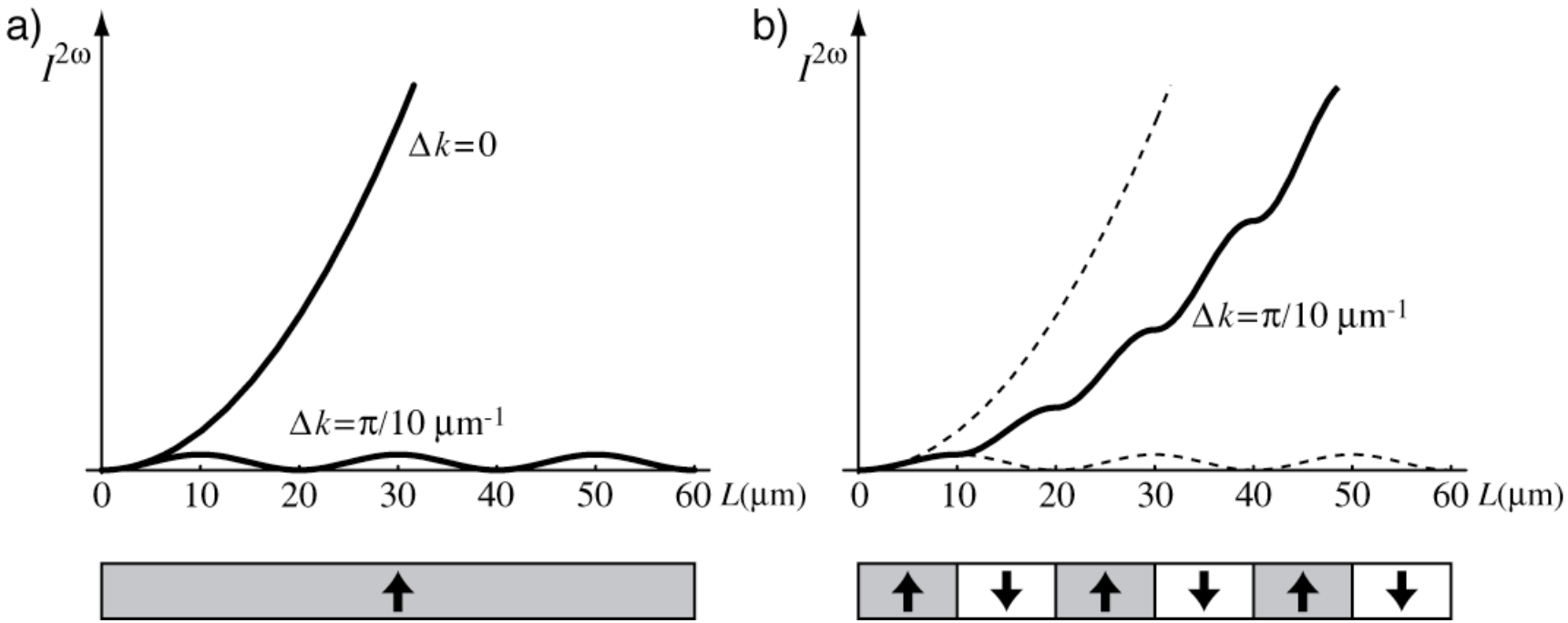

Figure15.8 Intensity of the second harmonic wave as a function of the propagation length *L* in a) homogeneously poled material with $\Delta k = 0$ and $\Delta k = \pi/10\ \mu m^{-1}$ b) periodically poled material with $\Delta k = \pi/10\ \mu m^{-1}$ and domain lengths of 10 μm.

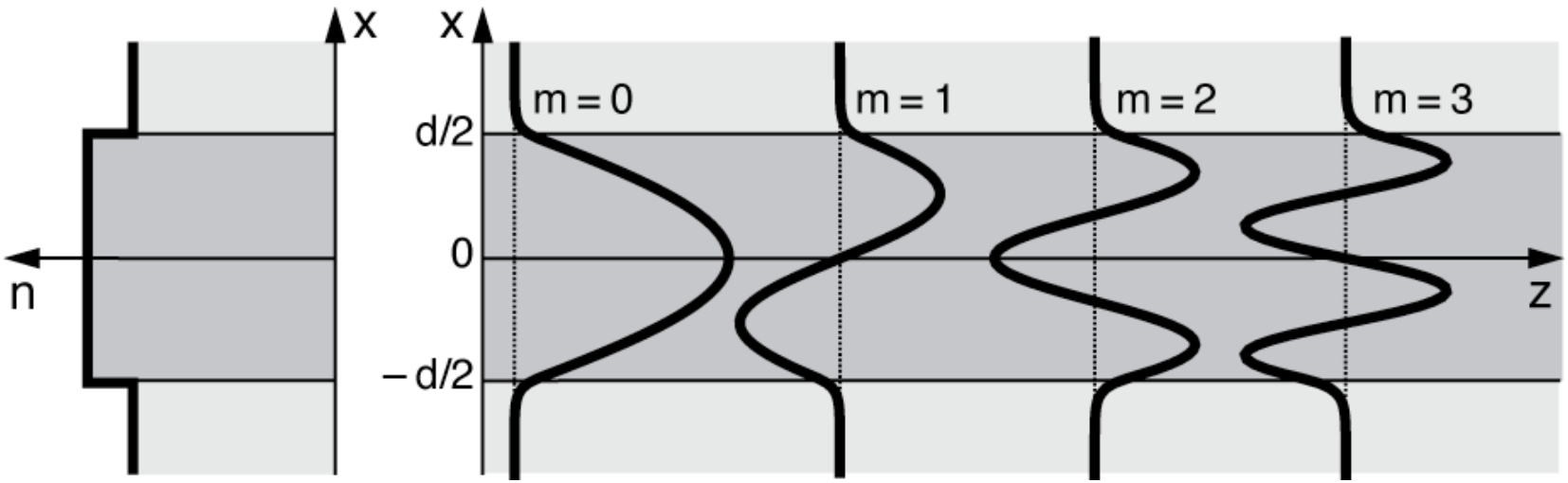

Figure15.9 Optical field profiles of the first four waveguiding modes m = 0,1,2,3 in a waveguide (right) with the refractive index profile that is shown on the left. The number of different modes supported by a waveguide depends on waveguide dimensions, refractive indices and light wavelength.

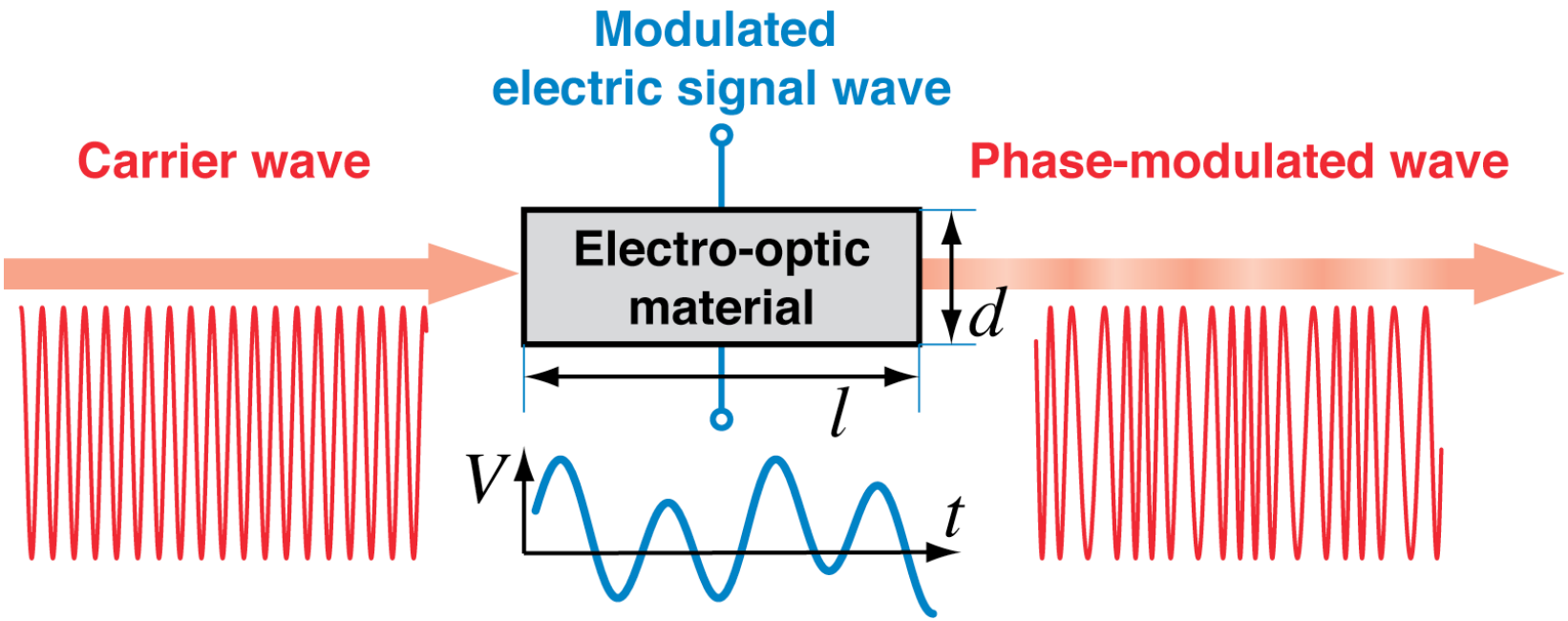

Figure15.10 Phase modulator: the phase of the output beam is controlled by the voltage applied to the crystal.

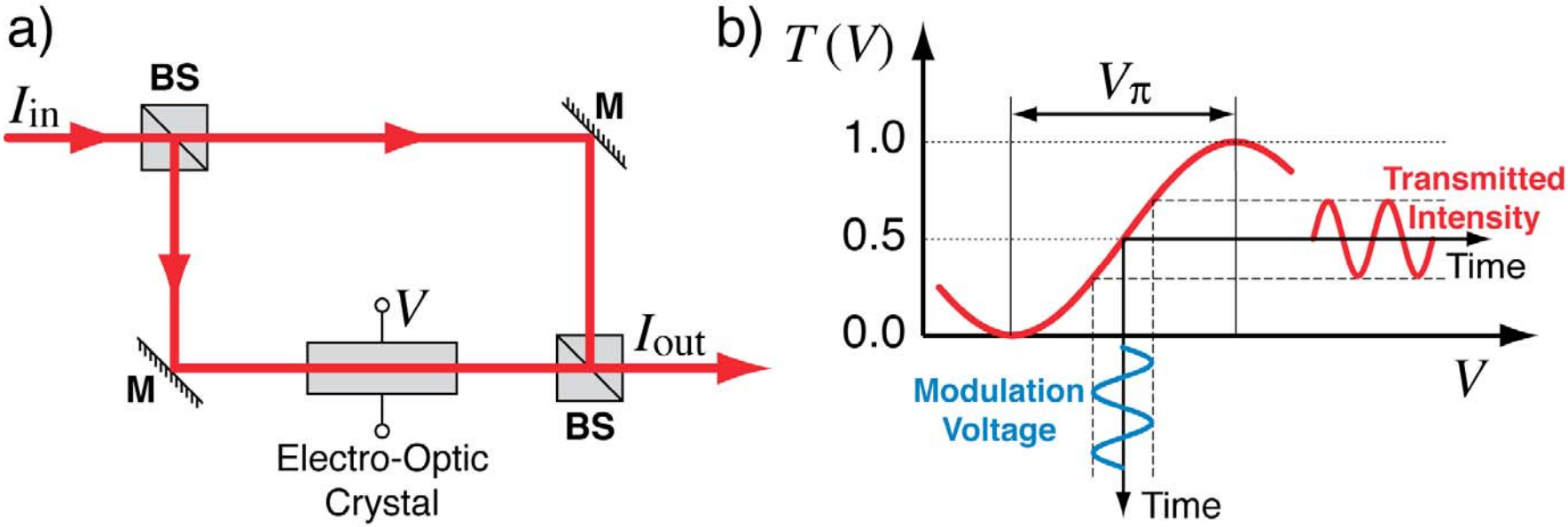

Figure15.11 a) Mach-Zehnder interferometer with a phase electro-optic modulator in one arm acts as an amplitude electro-optic modulator. BS: beam splitter; M: mirror. b) Transmittance of the interferometer as a function of the applied voltage.

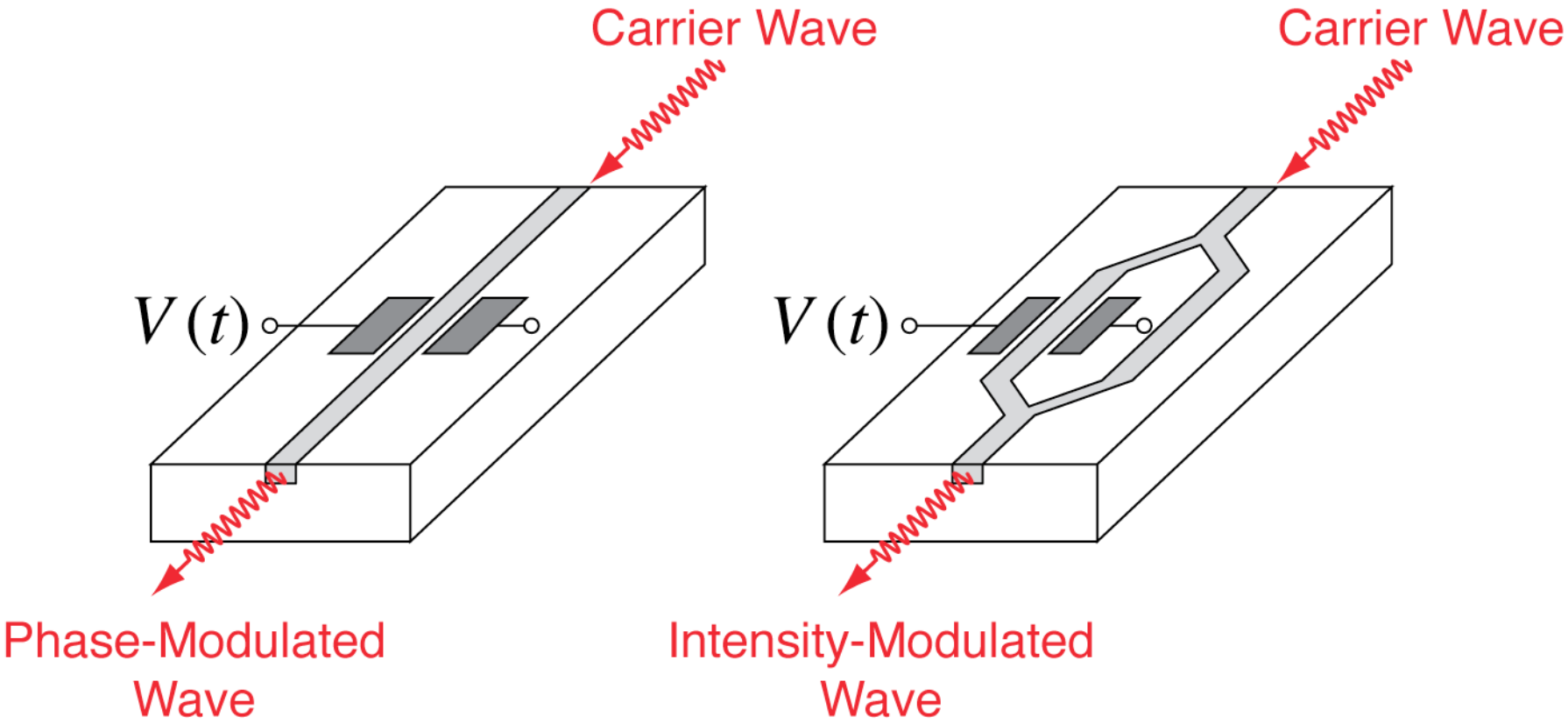

Figure15.12 An integrated-optics phase modulator (left) and a Mach-Zehnder intensity modulator (right) based on the electro-optic effect.

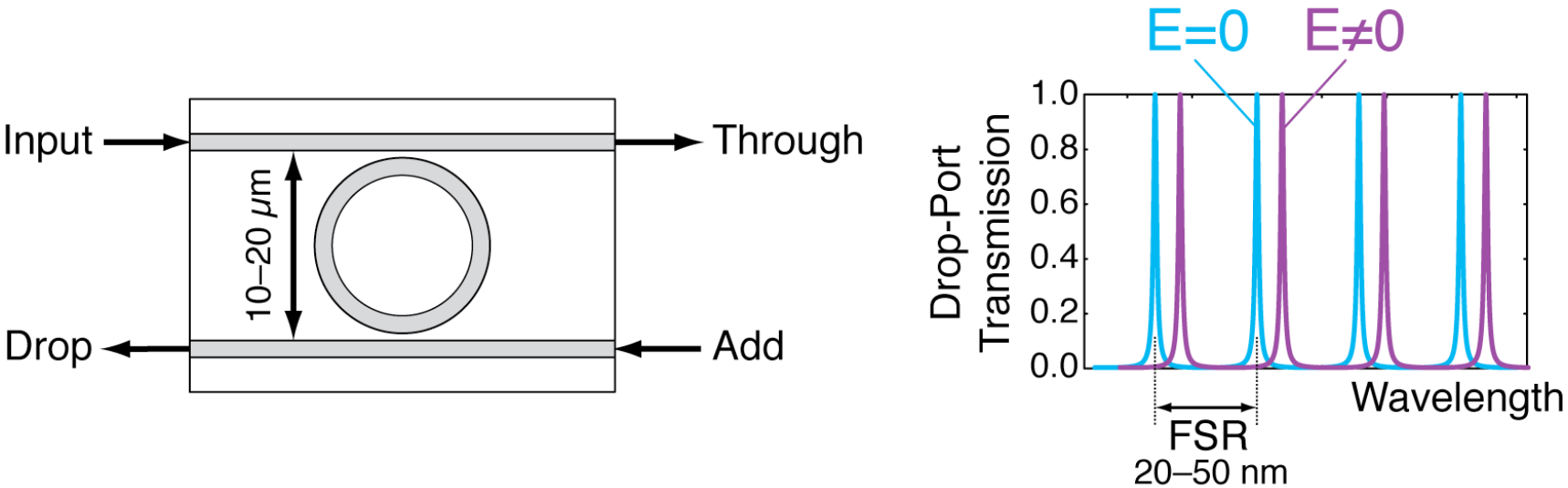

Figure15.13 A basic scheme of a VLSI microring device, viewed from the top (left). The device consists of two waveguides that are coupled by a microring waveguide. Light coming from the input-port waveguide will be transmitted through the through-port waveguide unless a resonance condition is met: in this case the intensity of light will increase dramatically inside the microring and will be coupled to a drop-port waveguide. Drop-port transmission is shown on the right as a function of light wavelength. The free-spectral range (FSR) is the wavelength separation between the adjacent transmission peaks. If the ring is made of an electro-optic material, we can tune its refractive index and therefore also the resonance condition by applying an external electric field.

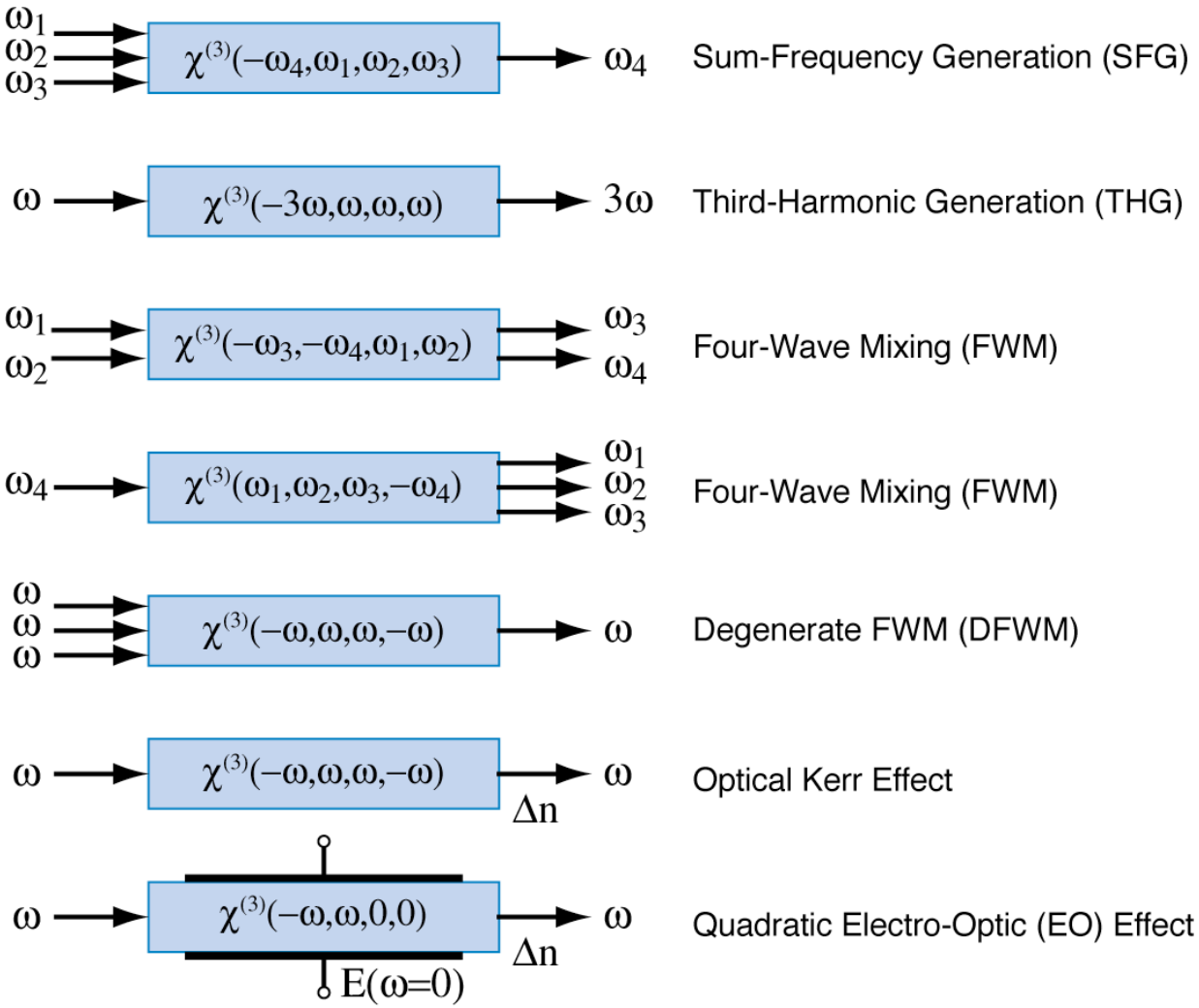

Figure15.14 Schematic representation of important nonlinear optical effects of the third-order, including the quadratic electro-optic effect.

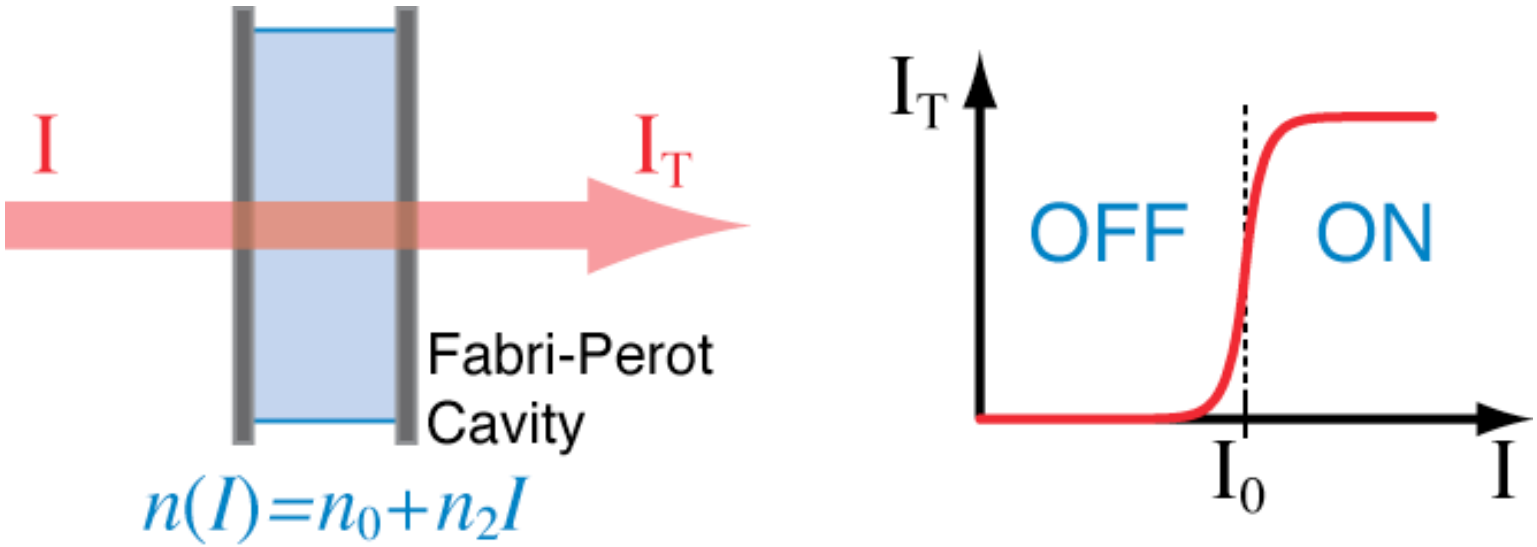

Figure15.15 Optical switching behavior, exhibited by a third-order nonlinear material in a Fabri-Perot interferometer.

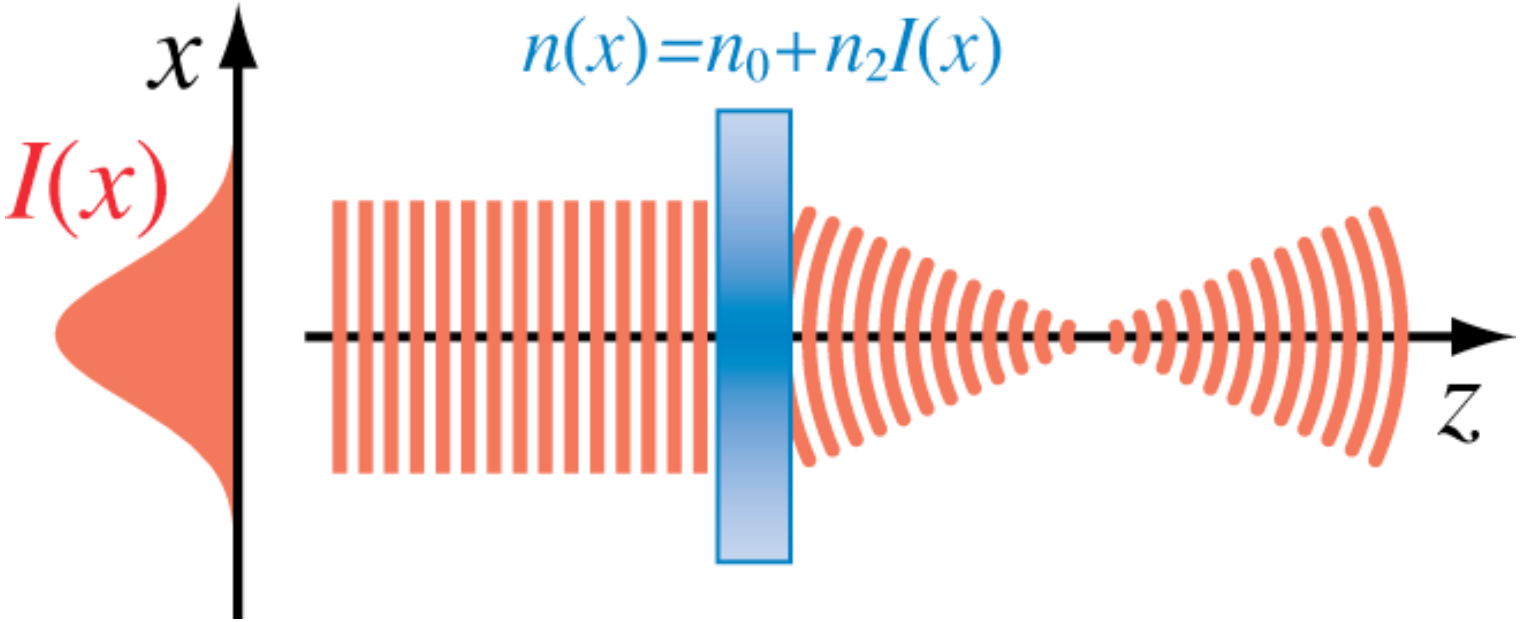

Figure15.16 Self-focusing effect of a beam with transverse intensity dependence.

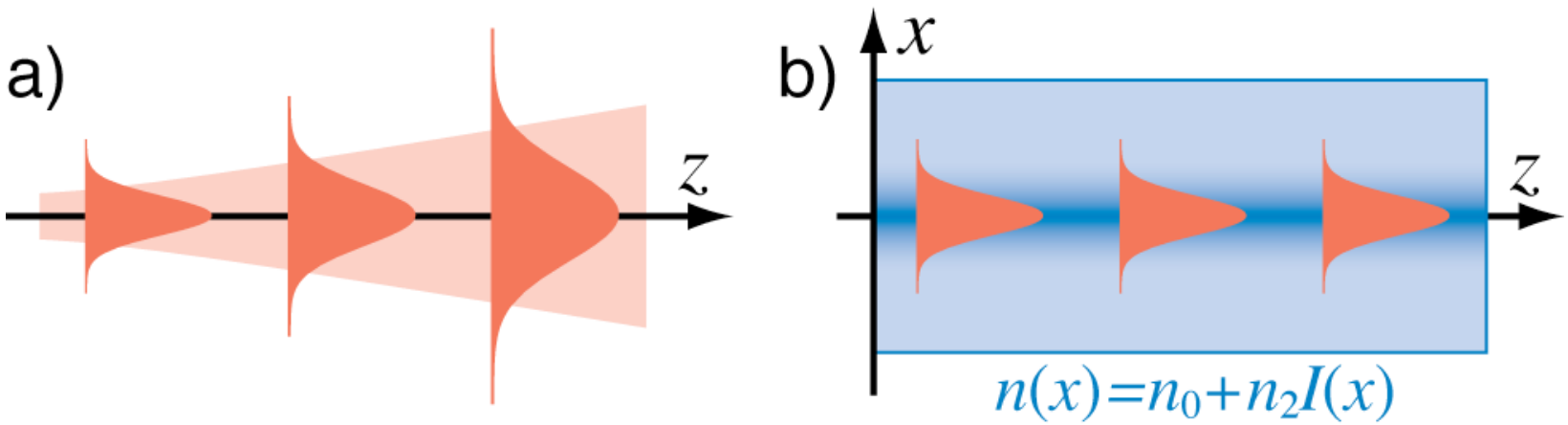

Figure15.17 Comparison between a) a Gaussian beam traveling in a linear medium, and b) a spatial soliton traveling in a nonlinear medium.

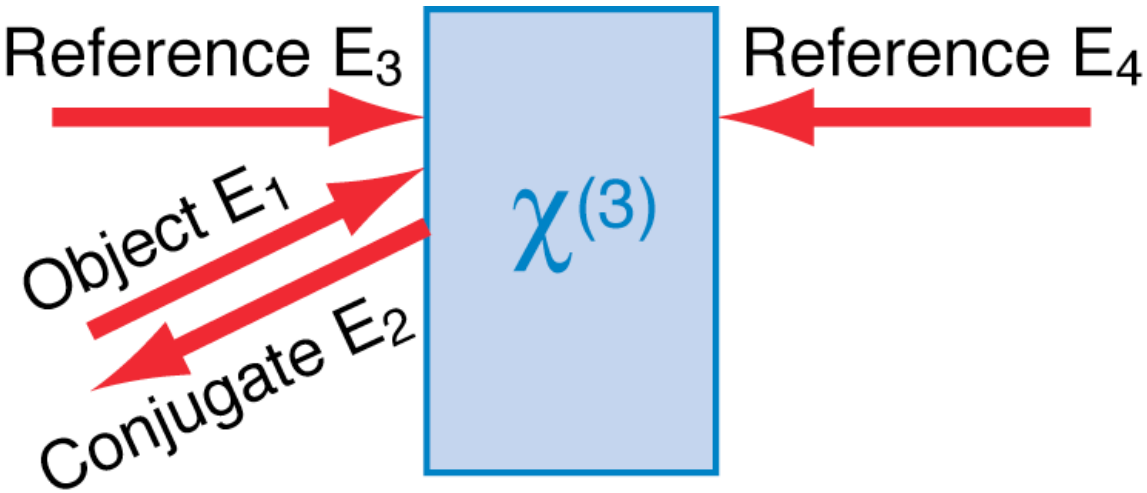

Figure15.18 Degenerate four-wave mixing configuration, in which the generated wave 2 is the phase conjugate version of the wave 1.

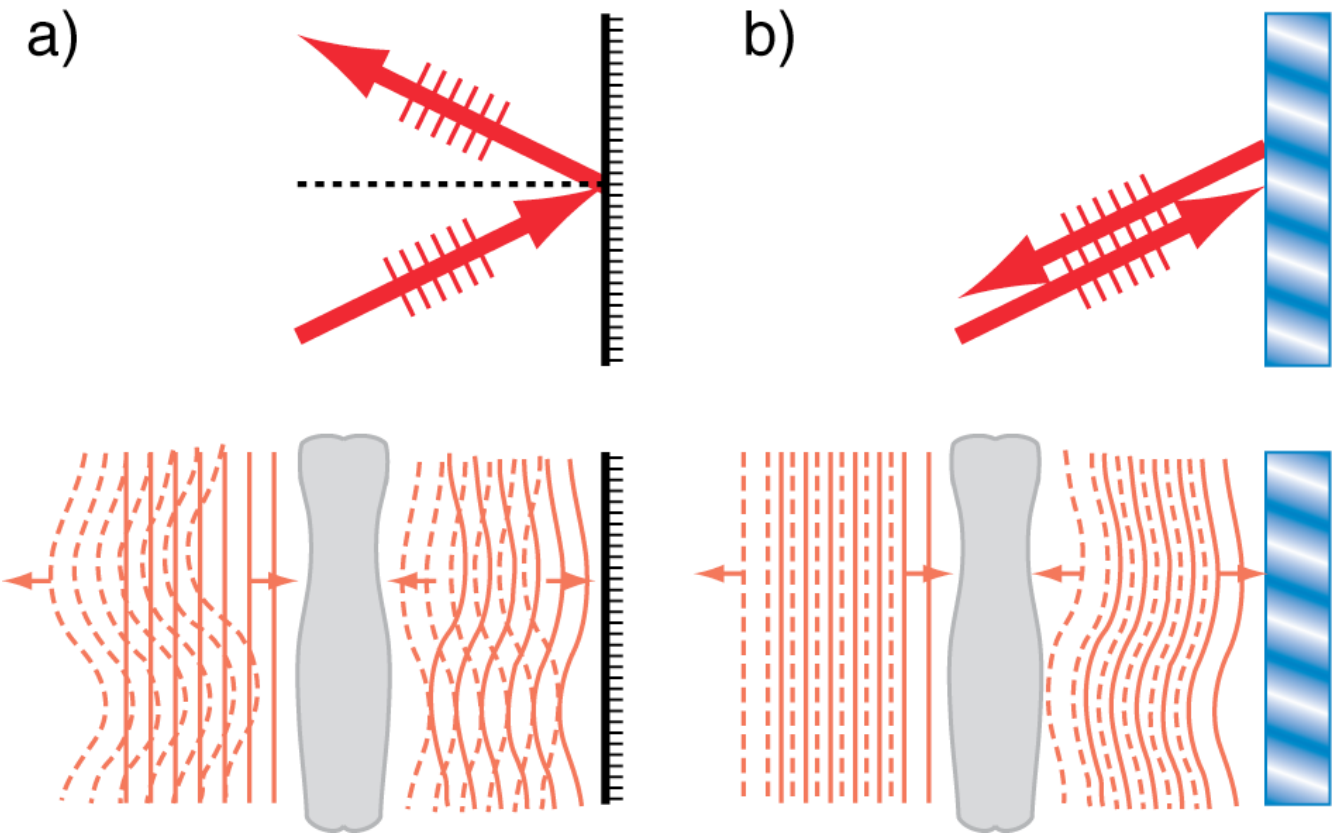

Figure15.19 Comparison between a) ordinary mirror and b) phase conjugate mirror. Phase conjugate mirror reflects the incident wave back to itself, so that it propagates exactly in the opposite direction (above) and compensates distorted wave fronts (below).

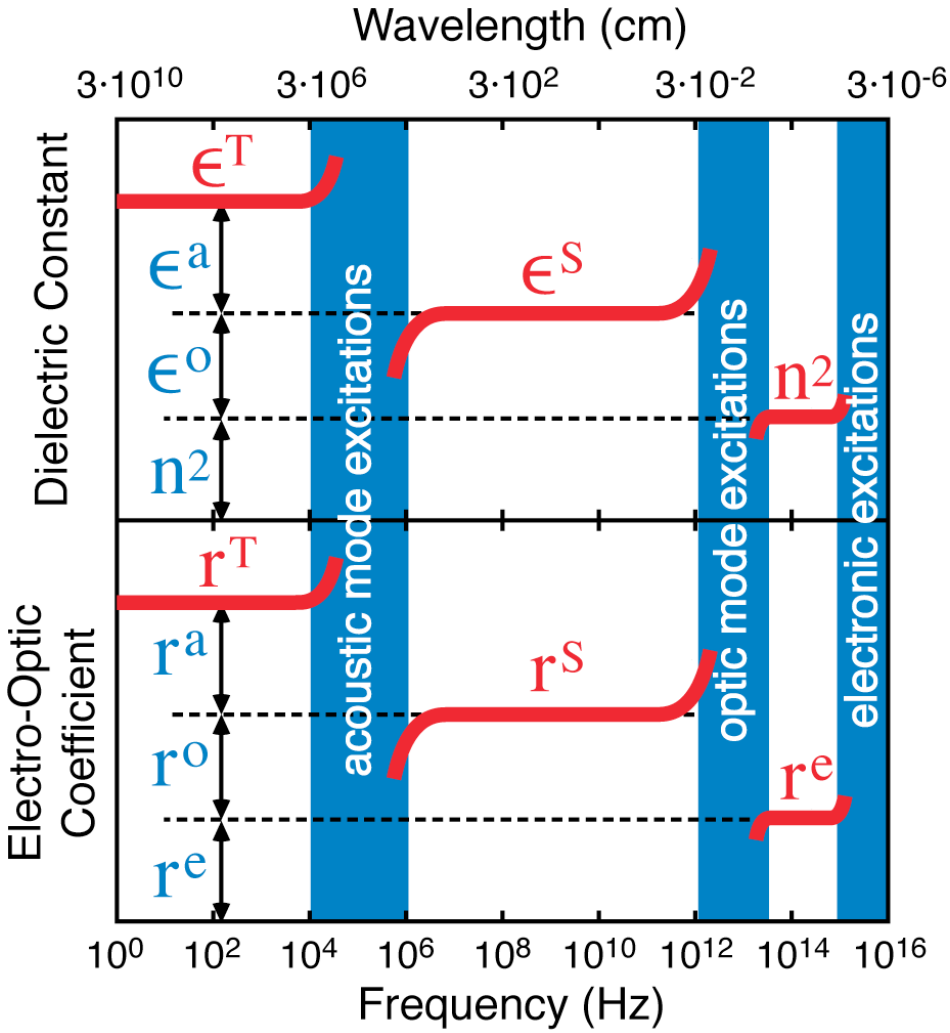

Figure15.20 Schematics of the material linear and of the nonlinear optical response as a function of the frequency of the external electric field.

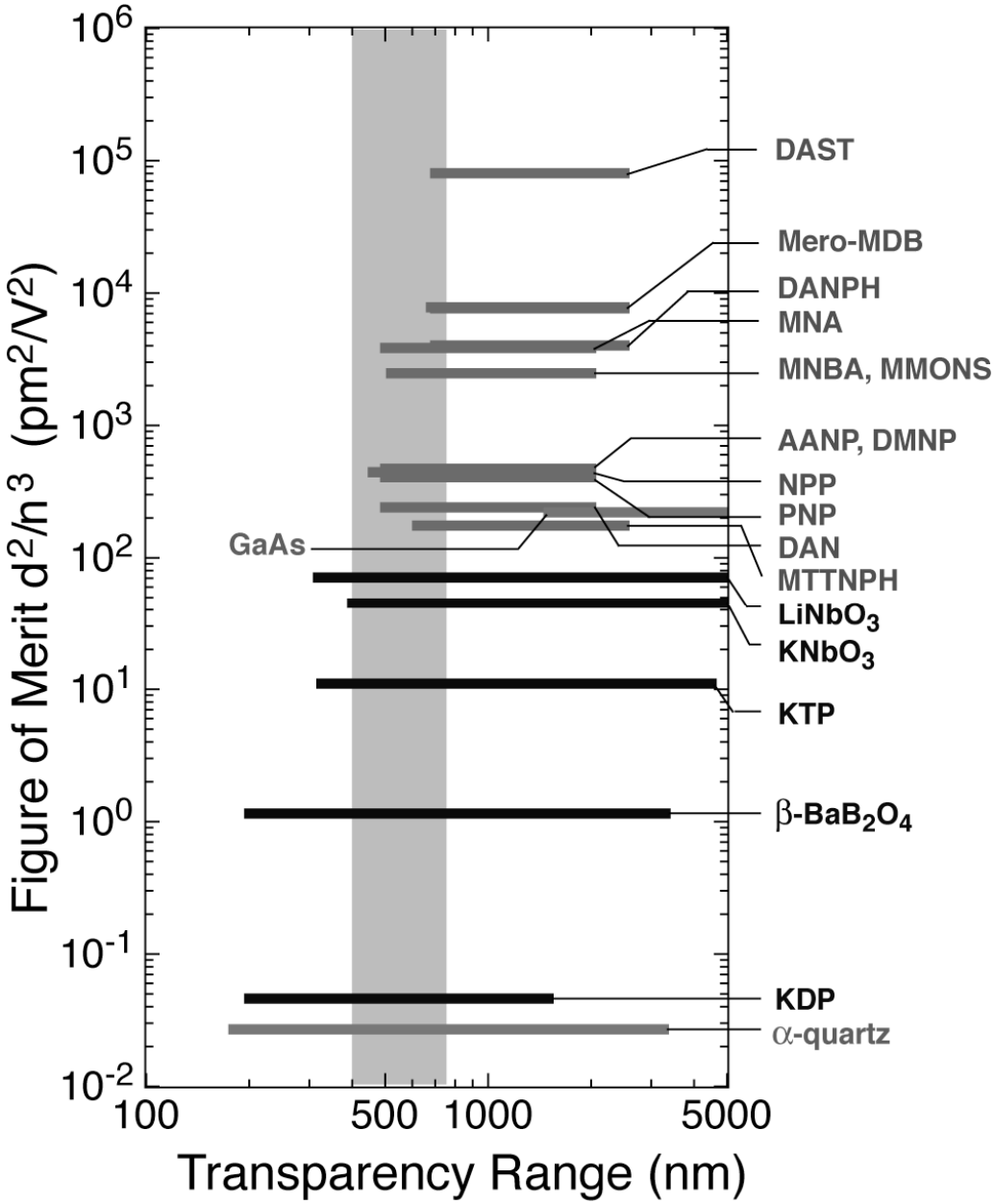

Figure15.21 The figure of merit for frequency doubling, d^2/n^3, versus the transparency range of various organic and inorganic crystals. The shaded area indicates the visible spectral range. Inorganic crystals are indicated in black, organic crystals in grey. It is clearly seen that organic crystals are much superior in terms of the figure of merit.

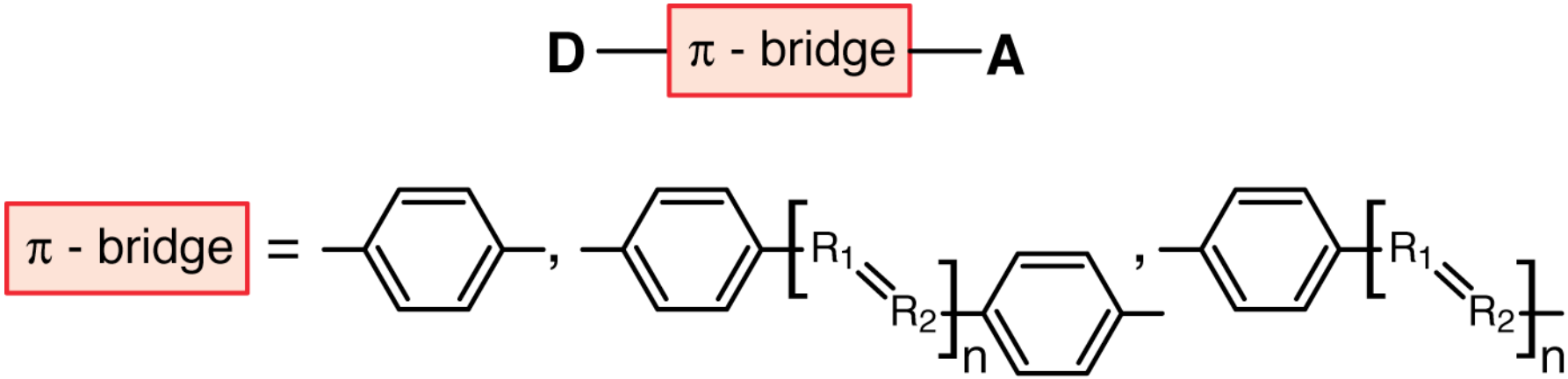

Figure15.22 Typical dipolar organic molecules for second-order nonlinear effects. The electron donor group (D) is connected to the electron acceptor group (A) through a π-conjugated structure. The most common systems are those containing one benzene ring (benzene analogs) and those containing two benzene rings (stilbene analogs). R_1 and R_2 are usually carbon or nitrogen.

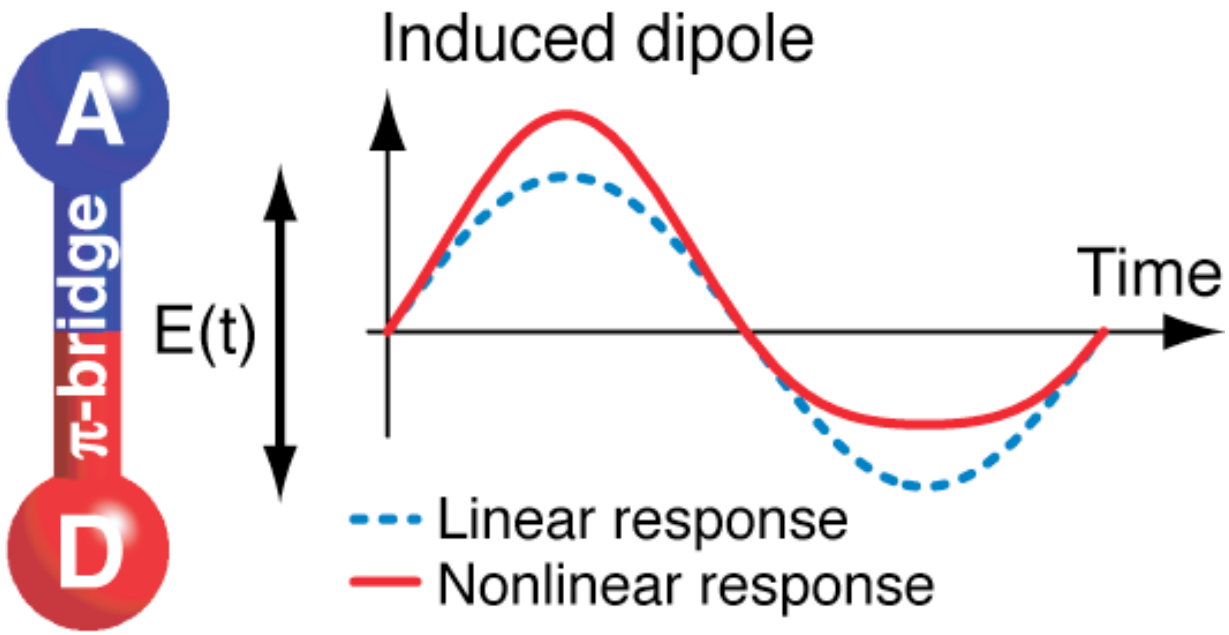

Figure15.23 Simple picture of the physical mechanisms of the nonlinearity of donor-acceptor π -conjugated molecules. If we excite such molecules with an optical field, we induce an asymmetric electronic response of the polarization. This is due to the nature of the substituents: the electron cloud (i.e. the electronic response) favors the acceptor over the donor.

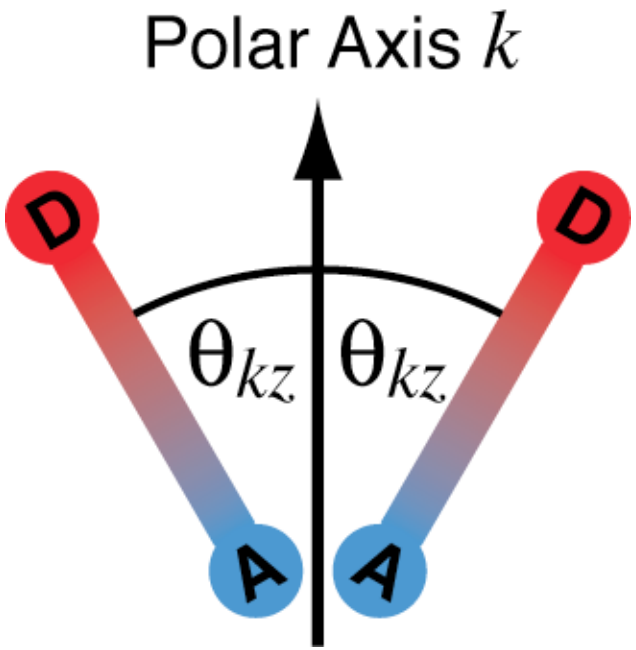

Figure15.24 Nonlinear optical molecules in the oriented-gas model. For phase-matched nonlinear optical applications the optimal angle θ_{kz} between the polar axis of the crystal and the charge transfer axes of the molecules is 54.7°, while for electro-optics the optimal $\theta_{kz} = 0°$.

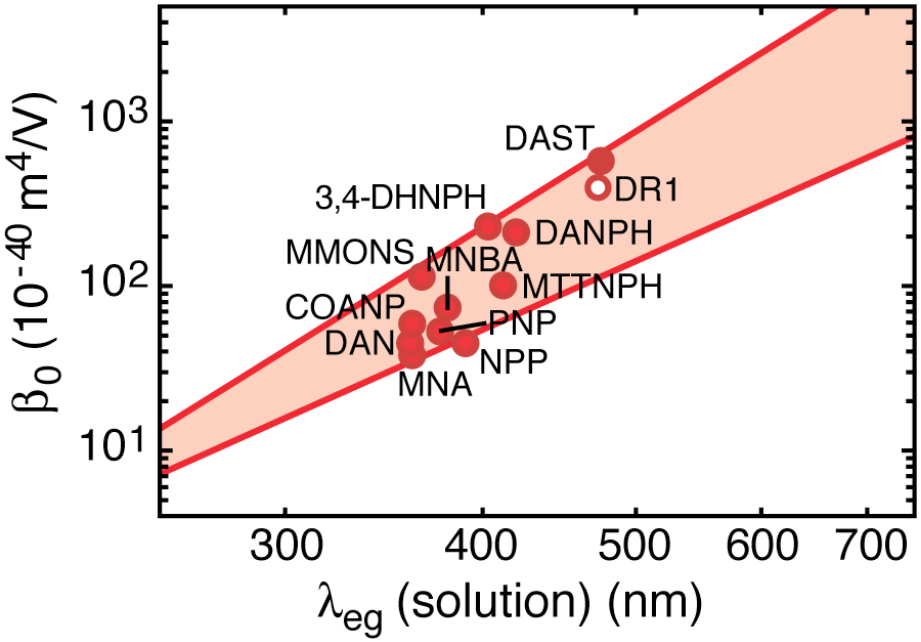

Figure15.25 First-order hyperpolarizability β_0 extrapolated to infinite wavelengths versus wavelength of maximum absorption for various molecules. The shaded area represents the range of values experimentally determined in various laboratories. For full names and molecular structures see Table 15.3. Acentric crystals are available for all chromophores included except DR1 (Disperse Red 1).

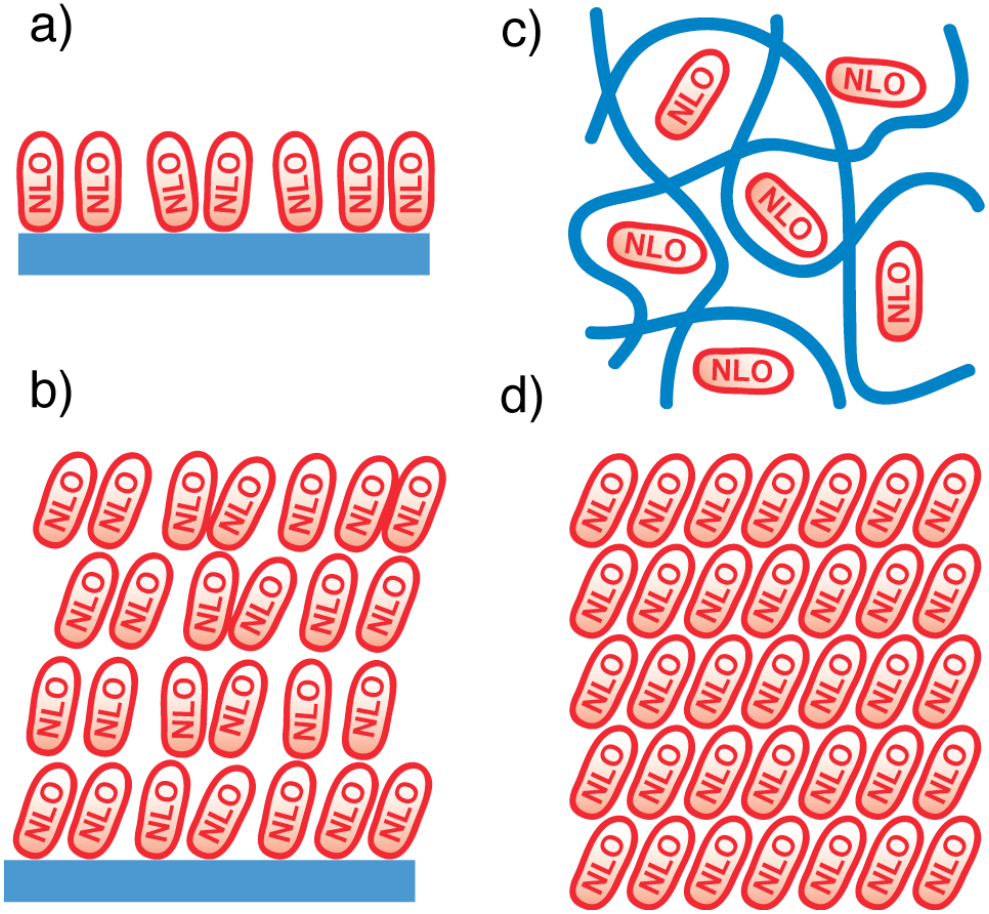

Figure15.26 Schematic illustration of different types of macroscopic second-order nonlinear optical organic materials based on π-conjugated dipolar molecules: a) Langmuir-Blodgett films, b) Molecular beam epitaxy, c) Poled polymers, and d) Single crystals.

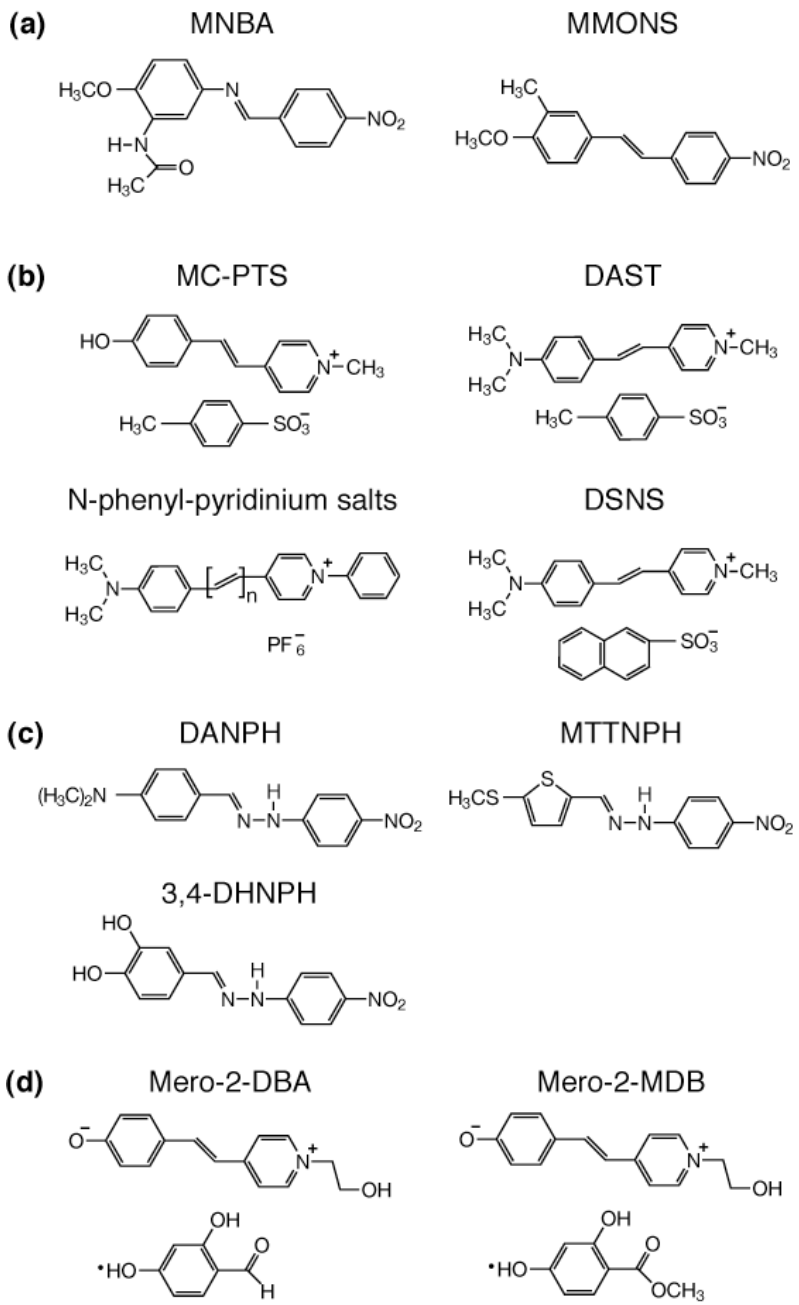

Figure15.27 Engineering strategies for inducing a noncentrosymmetric packing of nonlinear chromophores and examples: (a) use of molecular asymmetry, (b) use of strong Coulomb interactions, (c) use of non-rod-shaped π-conjugated cores, (d) supramolecular synthetic approach.

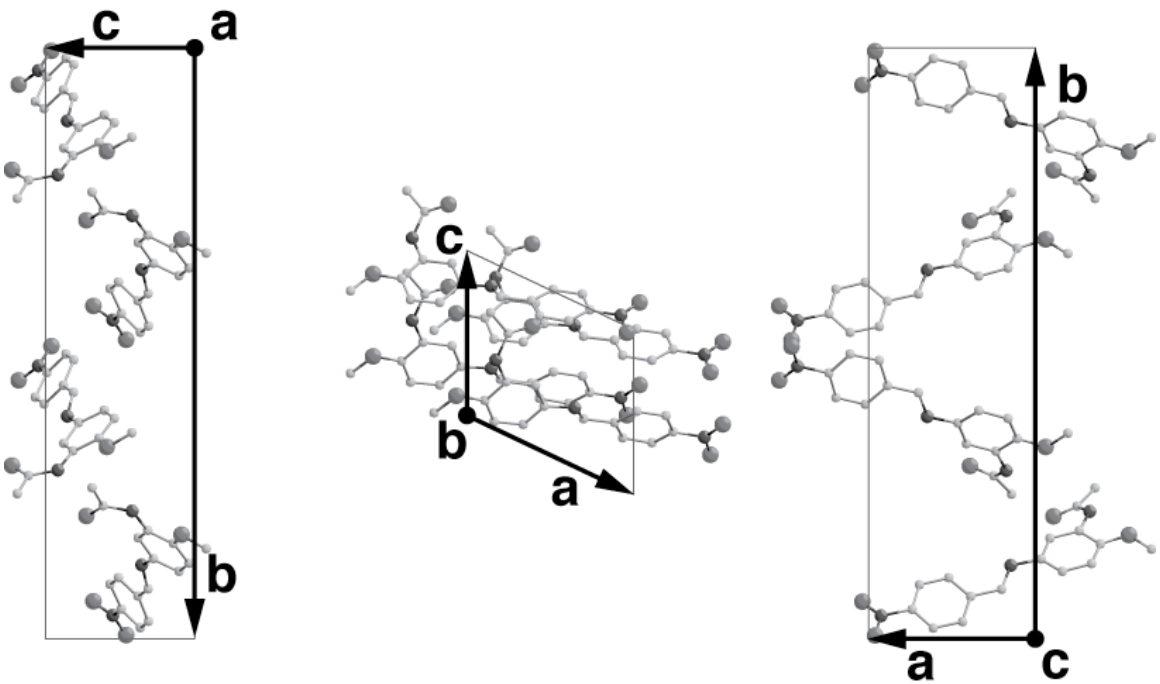

Figure15.28 Crystal structure of MNBA with the point group symmetry *m* projected along the crystallographic axes *a*, *b*, and *c* respectively. Hydrogen atoms have been omitted for clarity. The polar axis points approximately along the 4**a** + **c** crystallographic vector in the mirror plane that is normal to the *b* axis (projection in the middle). The angle between the long axes of the molecules and the polar axis is about 18.7º.

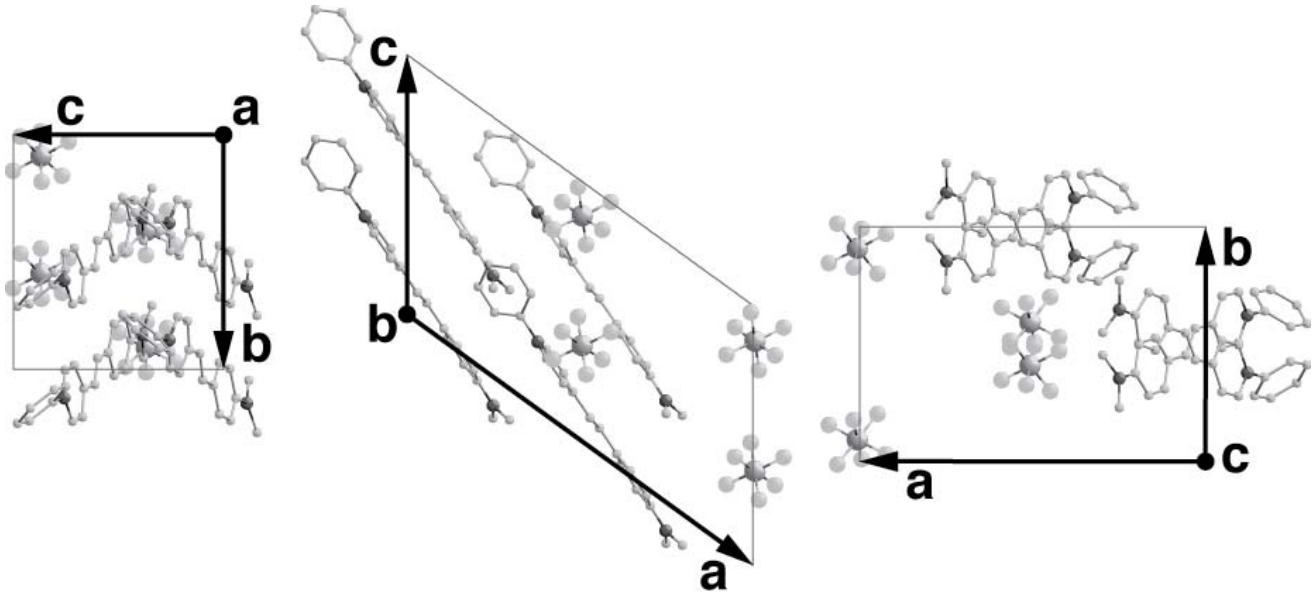

Figure15.29 Crystal structure of DAPSH with the point group symmetry *m* projected along the crystallographic axes *a*, *b*, and *c* respectively. Hydrogen atoms have been omitted for clarity. The polar axis points approximately along the **a** - **c** crystallographic vector in the mirror plane that is normal to the *b* axis (projection in the middle). The angle between the long axes of the molecules and the polar axis is about 15.5º.

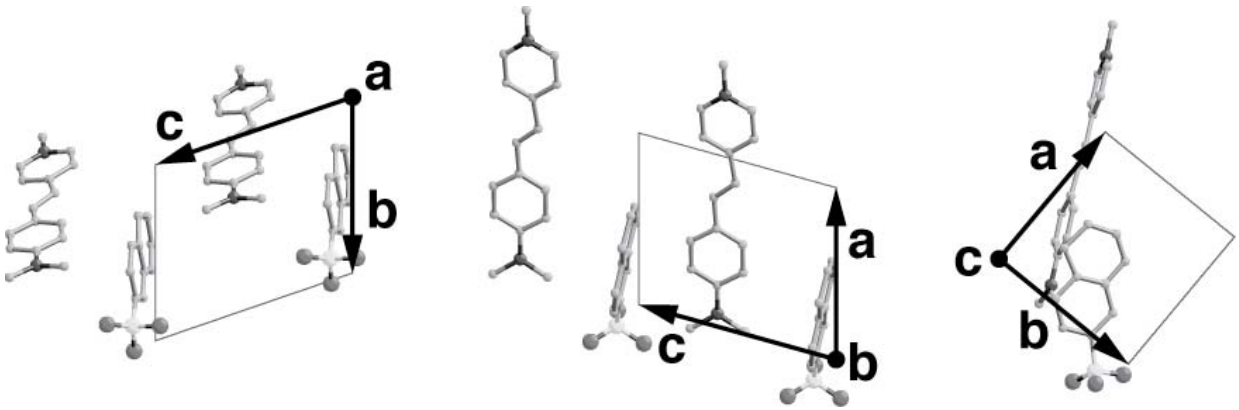

Figure15.30 Crystal structure of DSNS with the point group symmetry 1 showing molecules from two unit cells projected along the crystallographic axes *a*, *b*, and *c* respectively. Hydrogen atoms have been omitted for clarity. The polar axis points approximately along the 2**a** - **b** crystallographic vector (see the projection on the right). There is only one chromophore in the unit cell, meaning that all chromophores are perfectly parallel, leading to the optimal packing for the electro-optic applications with $\theta_{kz} = 0^\circ$.

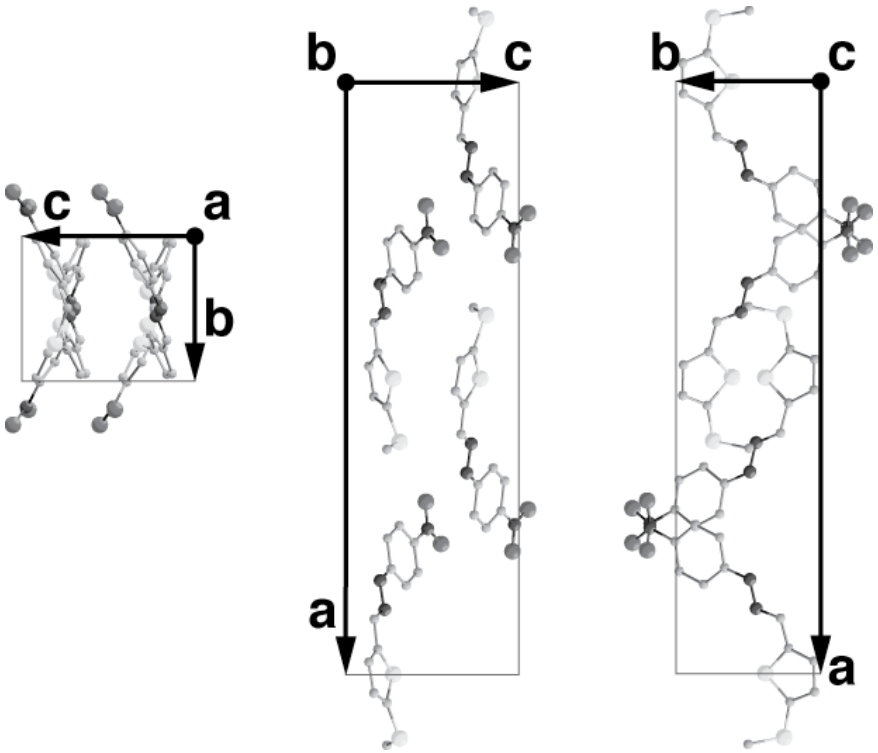

Figure15.31 Crystal structure of MTTNPH with the point group symmetry *mm*2 projected along the crystallographic axes *a*, *b*, and *c* respectively. Hydrogen atoms have been omitted for clarity. The polar axis points along the **c** crystallographic vector.

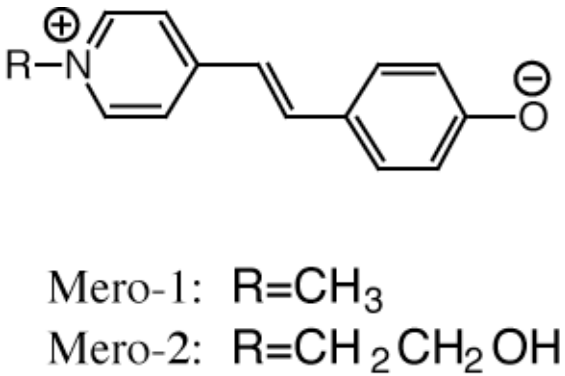

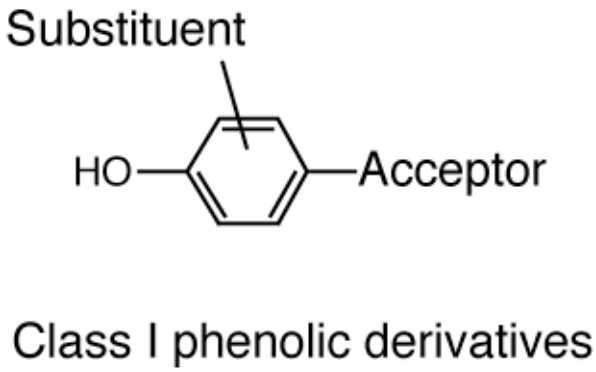

Figure15.32 Chemical structures of Mero-1, Mero-2, and Class I phenolic derivatives.

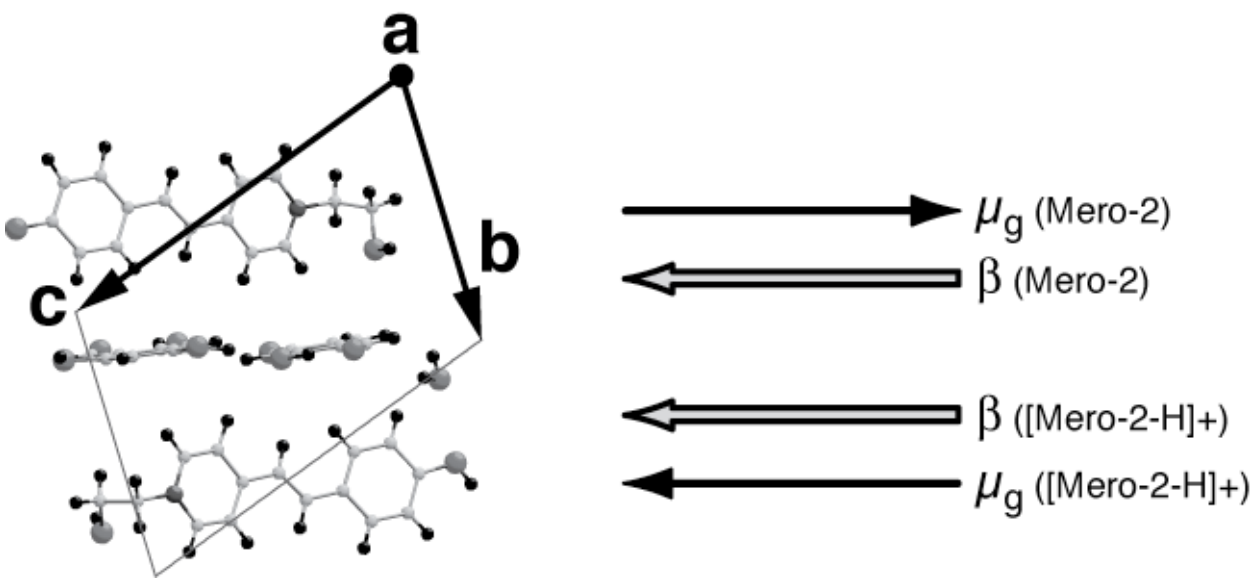

Figure15.33 Crystal packing of Mero-2-DBA crystal projected along the *a* axis with the directions of the ground-state dipole moments and the main directions of the first-order hyperpolarizabilities.

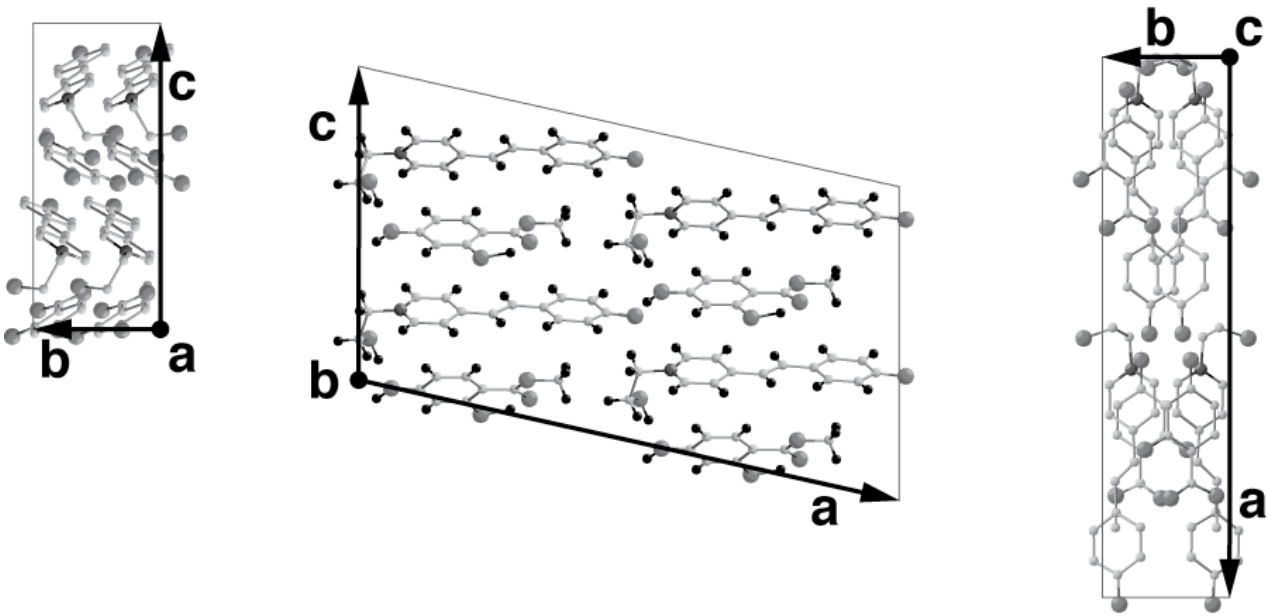

Figure15.34 X-ray structure of a hydrogen-bond directed, acentric layer structure of the co-crystal Mero-2-MDB projected along the crystallographic axes *a*, *b*, and *c* respectively. Hydrogen atoms are only shown in the projection along the *b* axis.

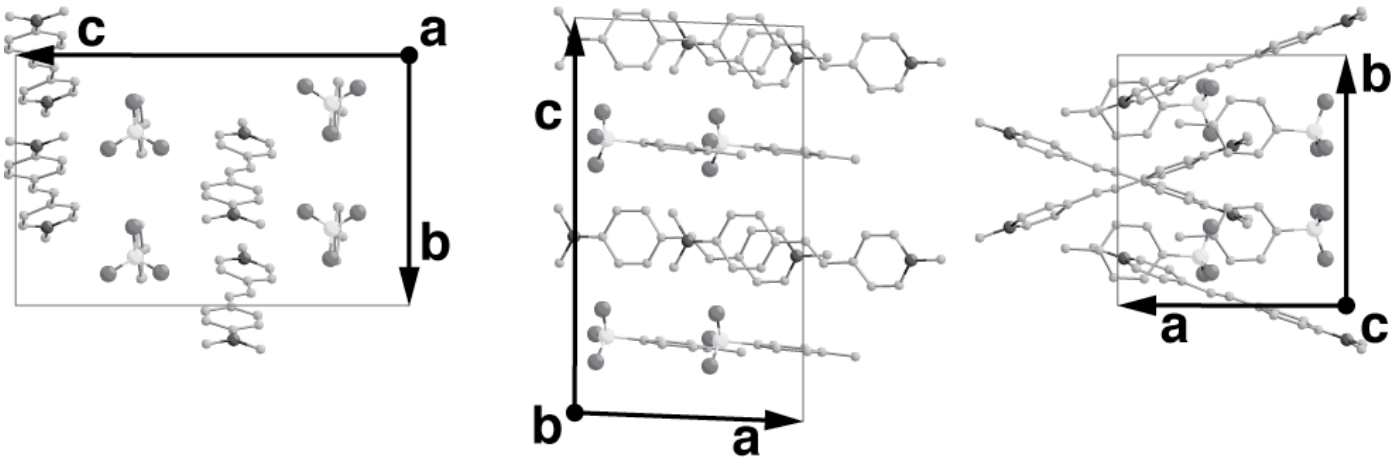

Figure15.35 X-ray structure of the ionic DAST crystal with the point group symmetry *m* showing molecules from one unit cell, projected along the crystallographic axes *a*, *b*, and *c* respectively. Hydrogen atoms have been omitted for clarity. The mirror plane is the *ac* crystallographic plane (projection in the middle). The chromophores make an angle of 20° with respect to the polar *a* axis (right).

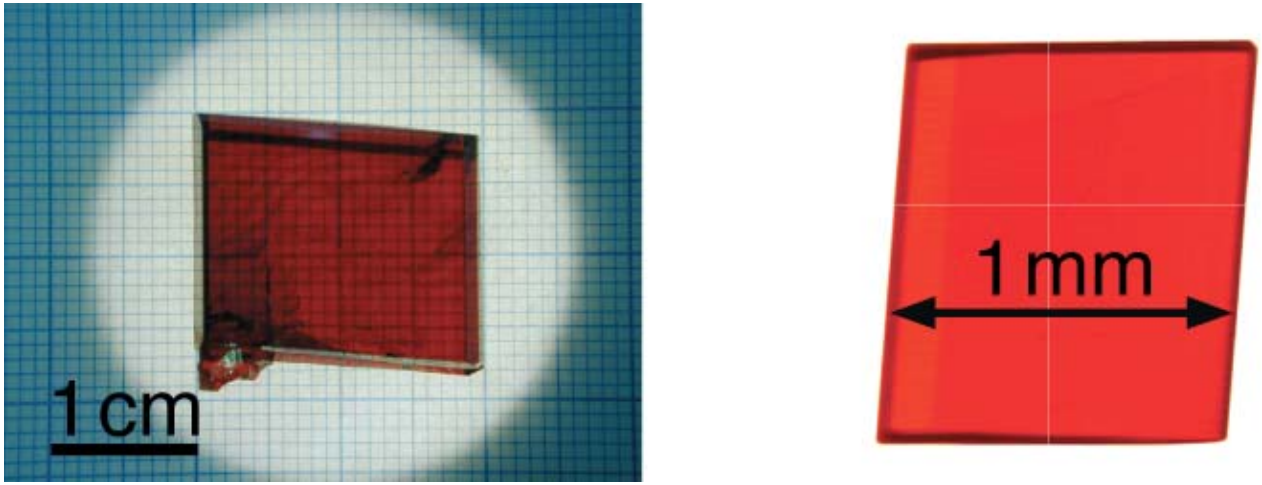

Figure 15.36 Bulk single crystal of DAST (left), grown from the solution by controlled temperature lowering technique, and a single-crystalline thin film (right), grown by planar solution growth.